CHEMISTRY OF MATERIALS

ARTICLE

pubs.acs.org/cm

Oxidation Dynamics of Epitaxial Rubrene Ultrathin Films

Enrico Fumagalli,[†] Luisa Raimondo,[†] Leonardo Silvestri,[†,‡] Massimo Moret,[†] Adele Sassella,[†] and Marcello Campione*[,§]

[†]Department of Materials Science, Via R. Cozzi 53, Milano I-20126, Italy

[‡]School of EE&T, University of New South Wales, Sydney, NSW 2052, Australia

[§]Department of Geological Sciences and Geotechnologies, Piazza della Scienza 4, Milano I-20126, Italy

Supporting Information

ABSTRACT: Great effort is being devoted to the fabrication of electronic devices based on rubrene thin films, because its outstanding charge transport properties make it one of the most promising organic semiconducting materials. Nonetheless, charge transport is strongly affected by the degree of crystallinity and degradation by photo-oxidation of rubrene. In the present work, in order to understand the dynamics of oxidation of rubrene when in the crystalline thin-film form, a combination of scanning probe techniques, such as Kelvin probe, phase contrast, and surface morphology atomic force microscopy, is used to study the oxidation process under ambient conditions of rubrene crystalline ultrathin films grown by organic molecular beam epitaxy on tetracene substrates. These films have a thickness of one or two molecular layers and consist of separated, island-like, epitaxial domains, whose orientation is determined by organic epitaxy. Theoretical calculations of the rubrene peroxide molecular dipole and structural data of rubrene and of purposely grown rubrene peroxide crystals, are exploited to determine the oxidation dynamics of such thin films and its connection with morphological, structural, and dielectric properties of the films. We demonstrate the formation of a native crystalline rubrene peroxide layer on top of the pristine rubrene crystalline domains.

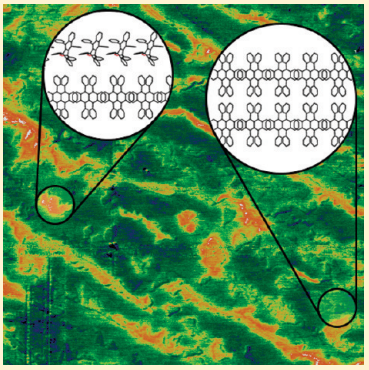

KEYWORDS: thin films, surface modification, organic electronics, epitaxy

1. INTRODUCTION

The past few years have seen a dramatic increase of interest toward the use of semiconducting organic materials to develop all-organic or hybrid organic−inorganic electronic devices, such as organic light-emitting diodes (OLEDs), organic field-effect transistors (OFETs), or photovoltaic cells.[1−3] Among these materials, much interest is devoted to rubrene (RUB, $C_{42}H_{28}$, 5,6,11,12-tetraphenyltetracene; see Figure 1a), which, in the single-crystal form, exhibits the greatest charge carrier mobility value among organic semiconductors.[4]

The great degree of miniaturization now required for the fabrication of electronic devices makes it necessary to grow RUB in crystalline thin-film form on different substrates.[5−7] Therefore, it is necessary to study the morphology and electric properties of such films and to determine their stability under ambient conditions. In particular, great attention must be devoted to the study of the dynamics and the effects of oxygen inclusion in solid films, when they are exposed to air. Indeed, it is well-known that RUB molecules undergo a fast oxidation process if exposed to air, and this process is strongly enhanced by light absorption.[8] Oxidation and photo-oxidation are particularly fast in RUB molecules in the gas phase, in solution or in amorphous films,[9] but it was shown that RUB single crystals or microcrystalline thin films also undergo oxidation.[10,11] In the latter case, the increased stability of RUB molecules in the crystalline phase limits this degradation process to the outermost molecular layers. Nonetheless, the oxidation of deeper molecular layers can be triggered by the exposure to light, and then proceeds even in darkness.[12] The main product of RUB oxidation is RUB endoperoxide (RUB-OX, $C_{42}H_{28}O_2$, see Figure 1b). RUB-OX molecules show electronic and structural properties strikingly different from those of nonoxidized RUB, mainly due to the disruption of the conjugate core of the molecule.[13,14] The way the presence of RUB-OX molecules in RUB crystals affects their electronic transport properties was already studied by different means. It was confirmed, both theoretically and experimentally, that the oxidation of RUB crystals leads to the formation of trap levels in the band gap of the material,[10,15,16] even though the actual effect of these trap states on the performance of RUB devices is still subject to debate. Indeed, conflicting experimental results, showing on the one hand an enhancement and, on the other hand, a reduction in conductivity, are reported in recent literature.[10,12,17,18] It is then evident that an in-depth knowledge of the actual mechanism of oxidation of crystalline RUB and of the way it affects its morphological and electrical properties is strongly worthwhile. Until now, the oxidation of RUB crystals and thin films was only studied on a macroscopic scale, by means of optical, electron, or mass spectroscopy, and, consequently, it was not possible to

Received: April 29, 2011
Revised: May 27, 2011
Published: June 13, 2011

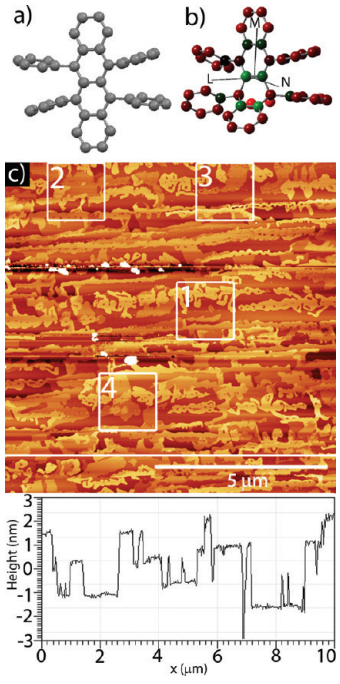

Figure 1. Ball-and-stick models of the molecular conformations of (a) RUB and (b) RUB-OX in their orthorhombic and triclinic (from dioxane solution) crystal polymorphs, respectively. The model in panel b is represented with a color scale evidencing partially negative (reddish) and positive (greenish) atoms, as obtained from Mulliken population analysis. (c, top) Morphological AFM image of a 10 μm × 10 μm area of the surface of a TEN single crystal covered by RUB islands, collected 80 min after exposure to air. The numbers identify four particular 1 μm × 1 μm areas of the image, whose evolution with time is reported in Figures 2 and 3. (C, bottom) Cross-sectional profile taken along the highlighted scan line.

observe the changes in the morphology of the thin film surface induced by the oxidation process.[9,11] Furthermore, in the case of thin films, the oxidation process was only studied on amorphous or polycrystalline phases, having a structurally and morphologically ill-defined solid film/air interface, and not on epitaxial crystalline films, having a complete textural and azimuthal order.

Here, we study the effects of the exposure to ambient conditions of crystalline ultrathin films (with a thickness of one or two molecular layers) of RUB, epitaxially grown via organic molecular beam epitaxy (OMBE) on a organic crystal substrate, which is a technique that leads to the formation of film phases with single-crystalline order.[19] For films of such a low thickness, the surface-to-volume ratio is maximized, thus enhancing the effects of the interaction with air and making them more easily noticeable. In addition, the presence of areas of bare substrate permits a direct comparison of the surface potential of RUB, which evolves with time, with the constant SP of the TEN crystal surface. By a combination of Kelvin probe force microscopy (KPFM)[20−22] and AFM morphology and phase contrast mapping with measurements and calculation of the electrostatic and structural properties of pure RUB-OX layers, we determine the oxidation dynamics of such films, in correlation with the evolution of their morphological, structural, and dielectric properties. Our results demonstrate that the oxidation of RUB crystalline ultrathin films leads to the formation of ordered crystalline layers of RUB peroxide. This also opens up an interesting scenario in the field of organic electronics, revealing the possibility to control the growth of a "native" crystalline oxide layer on the surface of a crystalline thin-film of an organic semiconductor. This prerogative allows us to predict RUB technology as being somehow similar to the well-assessed silicon technology, with the significative advantage of much lower process temperatures.

2. EXPERIMENTAL SECTION

Tetracene (TEN, $C_{18}H_{12}$, 2,3-benzanthracene) single crystals were grown from commercial powder (Sigma−Aldrich, 99.9%) by physical vapor transport at a temperature of 186 °C and with a constant nitrogen flux of 20 mL min^{-1}.[23] The crystals obtained expose the (001) surface, have a lateral size of few millimeters, and a thickness of some hundreds of nanometers. These crystals spontaneously adhere to the surface of the indium tin oxide (ITO)-covered glass that we used as a conducting substrate. The ITO layer used has a sheet resistance of 30−60 Ω sq^{-1} and a surface roughness of 3.6 nm (rms) over an area of 1 μm^2.

RUB ultrathin films with a nominal thickness of 1 nm were grown on the surface of the TEN crystals under ultrahigh vacuum (UHV) conditions (pressures of $<10^{-7}$ mbar) by OMBE.[19] During the growth process, the substrate is kept at room temperature. Commercial RUB powder (Acros Organics, 99%) was subjected to several sublimation cycles before using it as the source material. RUB is sublimated in a Knudsen cell at 160 °C to attain a deposition rate (as monitored by a quartz microbalance[24]) of ∼0.1 nm min^{-1}. When the growth process ends, the sample is brought to ambient pressure and, after a brief exposure to ambient light to trigger oxygen diffusion within the film,[12] is observed ex situ with a Nanoscope Multimode V (Veeco) atomic force microscopy (AFM) system, equipped with a "J" type piezoelectric scanner. The tips used to collect the images are silicon nitride tips coated with platinum (NT-MDT), with a typical force constant of 40 N m^{-1} and a tip curvature radius of 36 nm. To obtain KPFM images, the surface of the ITO-covered glass has been grounded by contacting it to the AFM scanner using conductive carbon paste. All the images were collected with a resolution of 512 × 512 pixels and with a scan rate of 0.7 Hz. KPFM images were collected in lift mode with a lift height of 5 nm, in order to maximize the lateral resolution.[25] All the measurements were performed under ambient light and in air, checking that no substantial variation of the measured surface potential occurred when a dry nitrogen atmosphere was used. Between successive measurements, the samples were kept under ambient conditions.

The analysis carried out on the collected AFM images were conducted with the SPM image analysis software Gwyddion (version 2.20)[26] and with the Nanoscope software (version 7.30). We estimated that, in our case, the typical statistical error in surface potential estimation using the KPFM technique is approximately ±40 mV.

RUB-OX single crystals used for crystal structure determination were grown from dioxane and from an anisole ($CH_3OC_6H_5$, methoxybenzene) solution via slow isothermal (22 °C) solvent evaporation. The RUB-OX solutions were obtained by photo-oxidation of 10^{-3} M RUB solutions kept in air under a halogen lamp (16 W). The complete oxidation, bringing to a colorless solution, was checked by a UV/vis spectrophotometer. The structure of the two single crystals was characterized by X-ray diffractometry. Data collections were carried out on a Bruker SMART APEX CCD diffractometer, using Mo Kα radiation (λ = 0.71073 Å). The structures were solved by applying direct methods techniques as developed in program SIR2004.[27] Full-matrix least-squares refinement with anisotropic displacement parameters for non-hydrogen atoms was applied with SHELXL-97.[28] In the case of RUB-OX crystallized from anisole, the solvent molecules were heavily disordered. The procedure SQUEEZE as implemented in program PLATON was applied to the diffracted intensities giving a substantial improvement on the structural refinement.[29] All hydrogen atoms were riding about their pertinent carbon atoms.

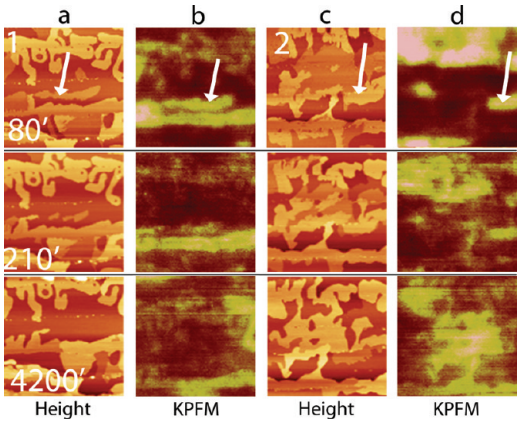

Figure 2. AFM morphology and KPFM images (1 μm × 1 μm) collected over areas 1 and 2 evidenced in Figure 1c: column a shows morphologic images of area 1; column b shows KPFM images of area 1; column c shows morphologic images of area 2; and column d shows KPFM images of area 2. From top to bottom, the rows respectively correspond to images collected 80, 210, and 4200 min after the extraction of the sample from the vacuum. The KPFM images potential scale is 200 mV. The arrows in the first row indicate specific features of the images, in order to make the comparison between morphologic and KPFM images easier.

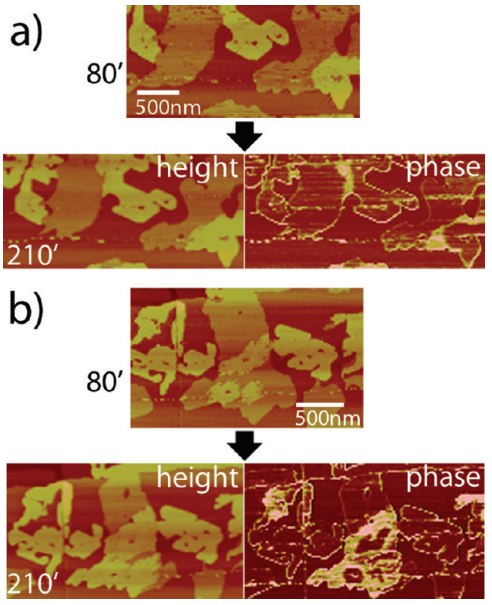

Figure 3. (a) (Top) Magnification of area 3 in Figure 1c, and (bottom) morphology (left) and phase contrast (right) images of the same area, collected 130 min afterward. (b) The same as that described for panel a, but for area 4 in Figure 1c.

The crystals obtained from dioxane have triclinic symmetry (space group $P\bar{1}$) with unit-cell parameters a = 7.62 Å, b = 11.16 Å, c = 22.66 Å, α = 101.70°, β = 94.31°, γ = 97.87°, and two molecules per unit cell. The crystals obtained from anisole have monoclinic symmetry (space group $P2_1/c$) with unit-cell parameters a = 11.26 Å, b = 21.33 Å, c = 13.62 Å, β = 101.80°, and four molecules per unit cell. CIF files are provided in the Supporting Information.

The electrostatic properties of RUB-OX molecules were determined by performing a density functional theory (DFT) calculation using the Gaussian03 software and employing the B3LYP hybrid functional along with the 6-31G basis set.[30] Ground-state properties of RUB-OX single molecule have been obtained by geometry optimization in vacuum, starting from the available atomic positions of RUB-OX in dioxane. The ground-state dipole moment has been found to be $\mathbf{d}$ = {−0.60, 1.04, −2.43} D in the L,M,N frame of reference of the molecular axis (see Figure 1b). Very similar results have been obtained starting from the slightly different geometry of RUB-OX in anisole.

3. RESULTS

3.1. Film Morphology and Its Time Evolution. Figure 1c shows the morphologic AFM image of a 10 μm × 10 μm region of the surface of a 1-nm-thick RUB film deposited on TEN(001), collected 80 min after the extraction from the growth chamber and the subsequent exposure to air. Observing the surface of the sample, one can notice the presence of surface steps of the original surface of the TEN crystal, roughly parallel to the horizontal axis of the image, and of RUB islands (the brighter areas of the image), some of which are lined up with the steps of the TEN surface. Magnifications of two of the areas evidenced in Figure 1c (areas 1 and 2) are reported, respectively, in the first and third columns of the first row of Figure 2. All the RUB islands have a molecularly flat surface, displaying a height of (1.4 ± 0.1) nm or (2.7 ± 0.1) nm, as can be seen from the cross-sectional profile reported below the image in Figure 1c. These two values match, within the experimental error, with integer multiples of the spacing between (200) planes of the RUB orthorhombic crystal (d_{200} = 1.343 nm).[31] Considering that (i) the surface of the islands is molecularly flat, (ii) their thickness is an integer multiple of the separation between (200) planes of orthorhombic RUB, and (iii) these planes separate single molecular layers, we can conclude that RUB islands are indeed crystalline, exposing the (200) surface of the orthorhombic phase. Within these domains, the principal molecular axis of RUB molecules is parallel to the substrate surface, in agreement with the results already reported in the literature.[5]

In columns a and c of Figure 2, the morphological time evolution of areas 1 and 2 in Figure 1c is shown. AFM images were collected, going from top to bottom, after 80 min (1.3 h), 210 min (3.5 h), and 4200 min (70 h) of exposure to air. It can be observed that the islands with a thickness of a single RUB molecular layer evolve in two different ways. They can either disappear, with the progressive migration and/or desorption of the constituting RUB molecules (as for the island indicated by the arrow in column a) of Figure 2), or they can be progressively covered by another layer of molecules (as the widest island in column c) of Figure 2). For most of the islands, however, we observed that the two processes occur simultaneously, with progressive erosion of the island borders and the formation of a new monomolecular layer starting from the central region of the island. These observations can be explained assuming that there is a mass transfer from the border of one-layer-thick islands to the top of them, until all islands have a thickness of approximately two molecular layers. Indeed, after enough time has passed (Figure 2, third row), all the islands that were previously only partially covered by a second molecular layer have reached a thickness of two molecular layers. Because of the long time that the sample is left unscanned between consecutive frames, we can definitely exclude a major effect of the scanning itself on the observed structural modifications.

In Figures 3a and 3b, morphologic and phase contrast images of areas 3 and 4 from Figure 1c, respectively, collected simultaneously

to those reported in the first two rows of Figure 2, are reported. While the substrate surface appears with dark contrast in the background of the phase images, RUB domains appear with two different contrasts. By comparison between the evolution of morphologic images and phase contrast images, one can realize that the molecular layers growing during observation appear with a bright contrast, whereas the surface of islands already present on the sample from the beginning appear with a dark contrast. Since, in general, collecting phase contrast images permits to distinguish areas of a surface with different structural and/or mechanical and/or chemical properties, this means that the new molecular layers forming in air are structurally and/or chemically different from those formed during film deposition under vacuum.[32]

3.2. Surface Potential Measurements. In columns b and d of Figure 2, KPFM images of the same areas shown in the morphologic images reported in columns a and c, respectively, and collected simultaneously to them, are reported. Comparing each KPFM image with the corresponding morphological image, some of the islands are observed to show the same surface potential (SP) as the substrate, while others have a higher SP value. In particular, while all the islands with the thickness of a single molecular layer do show a difference between their SP and that of the substrate, some of the thicker islands do not. As can be observed for the area indicated by the arrow in columns a and b of Figure 2, the areas of the substrate that become uncovered with time acquire the same SP of the rest of the substrate surface, while all the layers growing in air during observation have, from the beginning, a SP greater than that of the substrate (like the layer whose progressive formation is shown in columns c and d). In order to obtain quantitative and reliable data from KPFM measurements, one first must take into account the broadening effects due to the finite size of the tip and its long-range interactions with the sample. Indeed, the longer range of the electrostatic interactions involved in KPFM measurements, in comparison to the shorter range of the van der Waals interactions responsible for the morphology AFM imaging, leads to lower lateral resolution, and, for the smaller structures (with lateral dimensions on the order of the effective sample area interacting with the tip), to different measured SP values with respect to the real ones. Thus, there are two possible ways to obtain the actual SP values: (i) measuring the SP only on structures wider than the tip−sample interaction area; (ii) carrying out a deconvolution of the measured signal from the transfer function describing the tip.

When measuring structures with high aspect ratio, it is possible to carry out the deconvolution in one dimension, following ref 33, which greatly simplifies the required calculations. This can be done by fitting the KPFM profile of the structure with the following function:

$$Y = \Delta SP\left[\frac{1}{1+\exp\left(\frac{x-w_m/2}{d}\right)}\right]\left[\frac{1}{1+\exp\left(-\frac{x+w_m/2}{d}\right)}\right] + SP_2 \quad (1)$$

where $\Delta SP = SP_1 - SP_2$ (SP_1 is the absolute SP of the structure and SP_2 is the substrate absolute SP), w_m is the structure width (as measured from the topographic image), and d is a parameter that is dependent on the effective area of the sample interacting with the tip during the KPFM scanning ($w_{eff} \approx 4d$). If the uncovered substrate area surrounding the measured structure is large enough, the measured and effective SP values of the substrate are equal. Then, fitting the measured profile to eq 1, it is possible to determine both ΔSP and d.

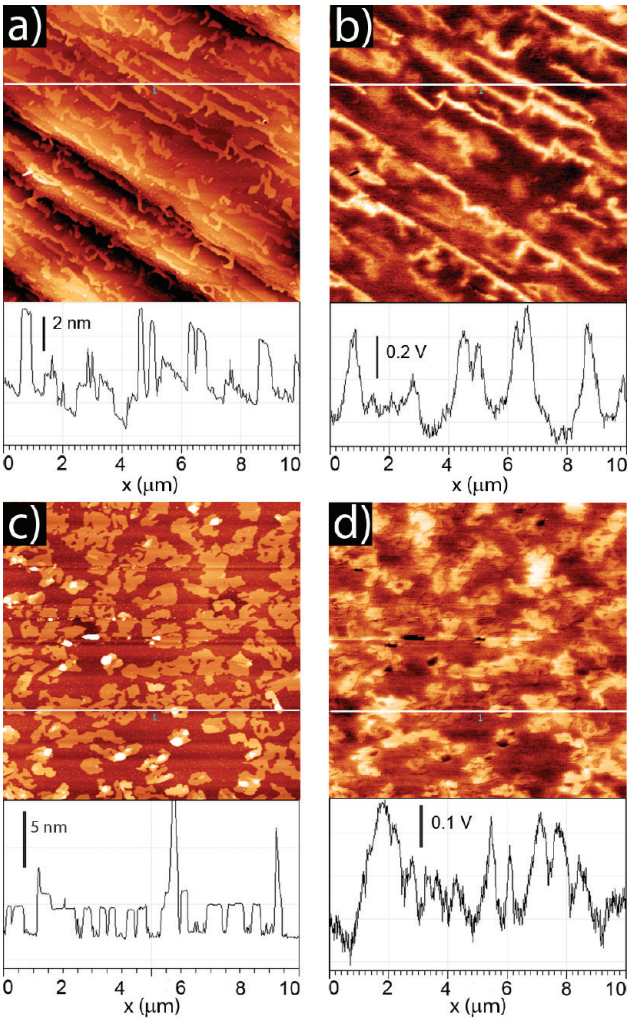

Figure 4. (a, c) Height and (b, d) surface potential maps of the surface of two different RUB ultrathin films deposited on TEN. Below each image, the cross-sectional profile taken along the highlighted scan line is reported.

Following this procedure for some of the structures with high aspect ratio in our KPFM images, we were able to determine that, under our experimental conditions, $w_{eff} \approx 200$ nm. Thus, it is possible to get reliable SP values from structures with a lateral size of >200 nm. Another effect to be considered when measuring the SP of a molecular layer with KPFM is the contribution of the polarization induced on the molecules by the potential applied between the AFM tip and the sample to the measured SP. However, in our case, the contribution of this effect to the measured SP can be neglected if compared to the contribution of the permanent dipole of the RUB-OX molecule.

Following these considerations, we were able to measure the actual values of the ΔSP between the islands and the substrate, by also performing KPFM measurements on other areas of the previously observed film and on other RUB films prepared under the same conditions, in order to get larger statistics. In Figure 4, some selected morphologic and KPFM images of the surfaces of the new samples are reported. It is worth noting that some TEN samples showed a low density of steps on their surface, enabling

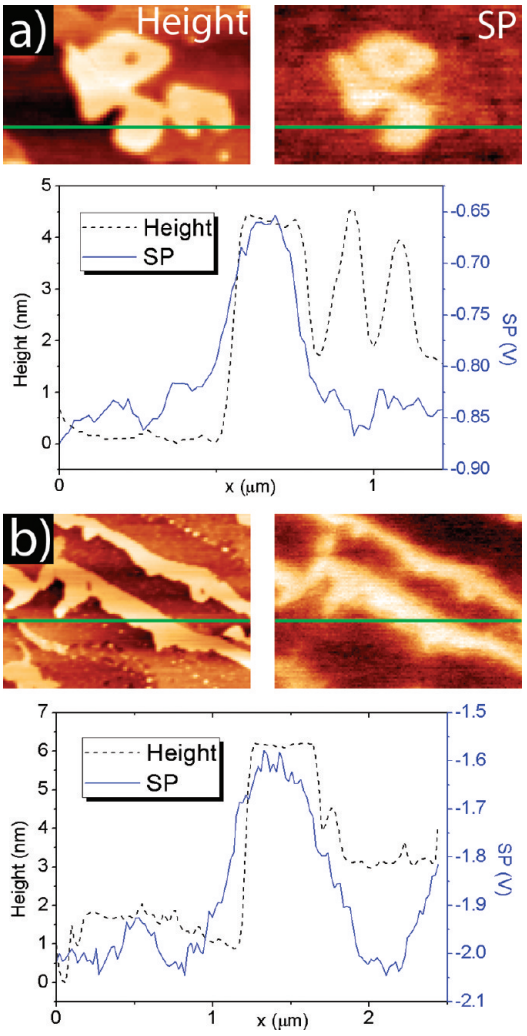

Figure 5. (a, b) (Left) Morphologic and (right) KPFM images of two selected RUB islands along with the respective cross-sectional profiles as taken along the highlighted scan line.

the growth of well-separated islands and then a more-accurate estimation of their potential (Figure 4c). The characteristics of the KPFM images are the same as those of Figure 2, described above.

The SP of the various islands is observed to be distributed around two values. In Figures 5a and 5b, the direct comparison of the KPFM and height images of two islands along with their cross-sectional profiles is shown. Considering all the ΔSP values measured for several islands of different films, we obtained the following estimates: $\Delta SP_1 = (0.20 \pm 0.04)$ V and $\Delta SP_2 = (0.42 \pm 0.04)$ V.

3.3. Crystal Structure and Electrostatic Properties of RUB-OX. All the morphological, physicochemical, and electrostatic transformations described so far are consistent with the formation with time of a foreign chemical species on the surface of the RUB crystalline domains, possibly induced by the sample interaction with air and ambient light. Having already been demonstrated that crystalline RUB oxidizes, we will now verify that what we are observing is indeed the progressive oxidation of RUB molecules to RUB-OX. This can be done by quantitatively comparing the data reported above with the structural and electrostatic properties of RUB-OX crystals and their differences with those of crystalline RUB. Thus, here, we present the results of the

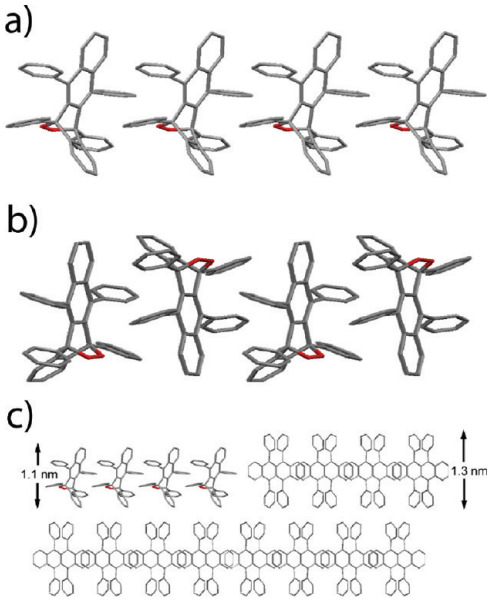

Figure 6. (a) Structural model of a molecular layer of RUB-OX molecules as arranged in the triclinic structure obtained from dioxane solution. (b) Structural model of a molecular layer of RUB-OX molecules, as arranged in the monoclinic structure obtained from anisole solution. (c) Structural model of a molecular layer of RUB-OX molecules arranged on the (200) surface of an orthorhombic domain of RUB.

structural characterization of RUB-OX crystals and of the calculations of their electrostatic properties, from which a full discussion of our results can be based.

RUB-OX can be obtained readily by exposure to light of RUB solutions; the reaction is complete when the solution presents negligible light absorption in the visible range. RUB-OX powder then can be obtained by recrystallization of the photo-oxidized product. Unfortunately, RUB-OX is thermally unstable, giving rise to a reddish product if heated above 160 °C. This prevents the possibility to grow single crystals of pure RUB-OX via thermal evaporation. Therefore, we explored many solution crystal growth methods, resulting in the identification of two crystal structures of RUB-OX. A triclinic structure was obtained for crystals grown from dioxane solutions and a monoclinic structure was obtained for those grown from anisole solutions. Regrettably, both types of crystals include solvent molecules; however, an interesting common feature of both structures is the presence of segregated monomolecular layers of RUB-OX, enabling the identification of a characteristic packing motif of aggregates of pure RUB-OX, which could eventually form on the surface of crystalline RUB thin films. Models of the molecule packing within monomolecular layers of RUB-OX are reported in Figure 6a and b, as extracted from the structures of single crystals obtained on the samples grown from dioxane and anisole solutions, respectively. Starting from these results, it is now possible to determine the electrostatic properties of RUB-OX layers.

In general, assuming an infinite homogeneous monomolecular layer, we can estimate the change in its electrostatic potential due to the dipole moment of the molecules to be

$$\Delta V = \frac{d\rho \cos(\theta_{tilt})}{\varepsilon_0}$$

dx.doi.org/10.1021/cm201230j |*Chem. Mater.* 2011, 23, 3246–3253

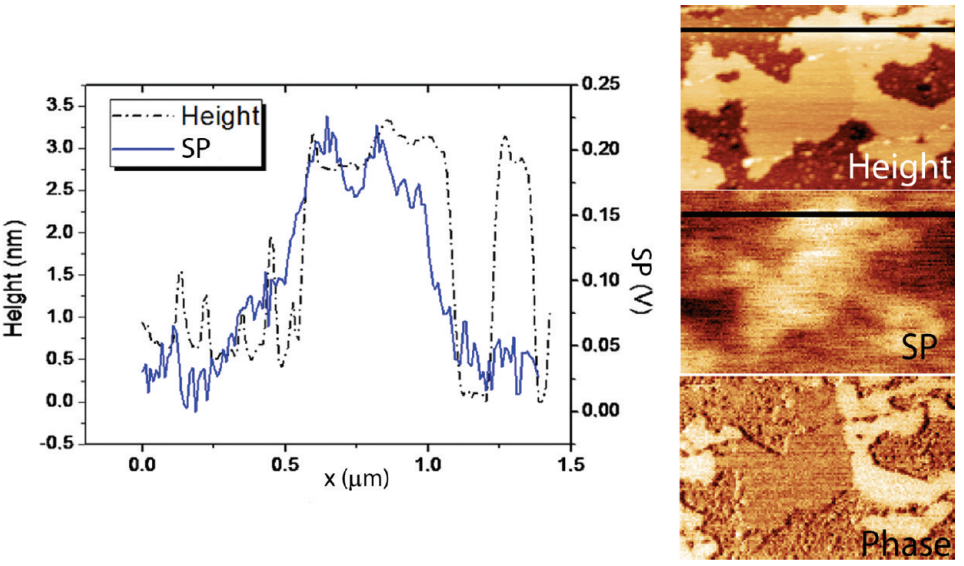

Figure 7. (Right) Three images showing, from top to bottom, a height image, a KPFM image, and a phase image of area 3 in Figure 1c, collected after 4200 min of exposure to air. (Left) Height (black line) and surface potential (blue line) profiles taken along the same highlighted horizontal scan line are shown.

where d is the molecular dipole, ρ the surface density of molecules, θ_{tilt} the angle formed by the molecular dipole with the surface normal, and ε_0 the vacuum permittivity.

From the crystallographic data of RUB-OX crystals grown in dioxane, considering an *ab* two-dimensional layer with one molecule per cell, we find $\rho \approx 1.2$ nm^{-2} and $\theta_{tilt} \approx 79°$, obtaining $\Delta V \approx 0.23$ V. The sign of the change in the potential depends on the orientation of the molecules; in the special case we considered, both signs are allowed, because of the presence of inversion symmetry in the packing structure. In the case of RUB-OX crystals grown in anisole, there are two molecules per two-dimensional cell whose dipole moments have opposite projections on the surface normal, thus producing no net change in the electrostatic potential of the layer.

4. DISCUSSION

In section 3.2, we have shown that, after sufficient time has passed from exposure to ambient conditions, all the observed islands have one of two possible ΔSP values, with respect to the substrate, namely, $\Delta SP_1 = (0.20 \pm 0.04)$ V or $\Delta SP_2 = (0.42 \pm 0.04)$ V. The smaller of these two SP values corresponds, within the experimental error, to the ΔSP value calculated in section for a single RUB-OX molecular layer packed following the triclinic structure of RUB-OX crystals grown from dioxane; the other ΔSP value is almost exactly twice the smaller one. The measured SP values then are compatible with the presence on the sample of islands comprising one or two molecular layers of RUB-OX packed following the triclinic structure shown in Figure 6a. This direct correlation between the presence of a layer of permanent dipoles on a surface and the SP shift determined by KPFM has been already exploited in the study of self-assembled monolayers formed on the surface of RUB single crystals.[34]

As shown in the previous section about RUB-OX structural data, the different configuration assumed by the oxidized RUB molecule leads to different lattice parameters between the RUB orthorhombic phase and the corresponding RUB-OX crystalline phase, in particular the triclinic one, leading to a matching with our findings about ΔSP. Therefore, if the observed ΔSP values are due to the presence of RUB-OX, there should be a thickness difference between islands showing a nonzero ΔSP and islands with zero ΔSP. In particular, a different interlayer spacing between the RUB orthorhombic crystal and the RUB-OX phase (Figure 6c) should be found. As can be observed in Figure 7, which reports the height, KPFM, and phase contrast images of area 3 in Figure 1c (collected after 4200 min of exposure to air), differences in the SP and phase contrast correspond to a difference in the height of the island. In particular, the superposition of the height and the SP profiles collected along the same scan line shows that an increase of the SP does correspond to a decrease in the height of the island. Measuring the height difference between adjacent zones, which show both a different SP and a different phase contrast, we obtain an average value of (0.25 ± 0.02) nm, which is compatible with the value calculated from the known crystalline structure of RUB-OX (Figure 6c). This result corroborates the assumption that what we are observing are indeed crystalline RUB-OX molecular layers nucleated on top of crystalline RUB domains.

Finally, it is possible to propose a feasible mechanism leading to the oxidation of epitaxially grown RUB thin films. It is known that, while amorphous RUB films tend to completely oxidize very rapidly, RUB single crystals do not, being the presence of RUB-OX limited to the outermost molecular layers.[11] In full agreement with these findings, we found here that RUB epitaxial domains with a thickness of two or more molecular layers behave as single crystals, oxidizing very slowly, in comparison to the one-layer-thick domains. In addition, the latter are also morphologically unstable, as demonstrated by the transfer of mass from their borders to their top, until a more-stable configuration is reached. Afterward, RUB molecules from these less-stable layers oxidize, concurring to form new molecular layers entirely constituted of RUB-OX molecules, which arrange according to the RUB-OX single-crystal structures. Nonetheless, after enough time has passed, also the thicker islands oxidize, as can be noticed in Figures 4b and 4d, where all the islands have a positive ΔSP. This observation is also in accordance with the literature, which shows

the presence of RUB-OX in the outermost layers of RUB monolithic crystals.[11] Finally, the positive sign of the measured ΔSP indicates an arrangement with the oxygen atoms pointing downward, as depicted in the model in Figure 6c. These newly formed layers appear to be stable, possibly due to the interaction of both hydrogen and oxygen atoms with the (200) surface of RUB domains, enhancing surface adhesion. Such a stability is definitely a very positive property, which permits one to envisage a future RUB-based technology in organic electronics.

5. CONCLUSIONS

The oxidation dynamics of rubrene (RUB, $C_{42}H_{28}$, 5,6,11,12-tetraphenyltetracene) crystalline ultrathin films epitaxially grown on tetracene (TEN) substrates and consisting in separated, highly crystalline, island-like domains, was observed in real time, thanks to the combined use of different atomic force microscopy (AFM)-based imaging techniques, such as Kelvin probe force microscopy (KPFM), phase contrast, and topographical mapping. We demonstrate the formation of a crystalline RUB peroxide layer above the pristine RUB epitaxial domains, occurring through a mass-transport process from unstable monomolecular RUB layers toward more-stable bilayer and multilayer domains. We believe this mechanism is not limited to submonolayer thin-film phases, but it is also active on the surface of thicker films and single crystals at defect sites such as vacancies and step-edges. In-depth knowledge of the oxidation process of such materials, especially when in the crystalline phase, and of its effects on their physical properties, is a key requirement for further developments of all-organic electronic devices such as organic light-emitting diodes (OLEDs), organic field-effect transistors (OFETs), and photovoltaic cells. Indeed, these devices should be able to work under ambient conditions for everyday use, and then their behavior under those conditions must be fully understood. In particular, the oxidation of RUB has a dramatic effect on the charge transport properties of RUB-based devices; thus, better knowledge of the actual mechanism of crystalline RUB oxidation will help the understanding of how it affects those properties and how to control them. In addition, the use of organic semiconducting materials with a stable native oxide surface layer could permit the exploitation of technologies already well-assessed in the field of inorganic semiconducting materials such as silicon.

■ ASSOCIATED CONTENT

Supporting Information. CIF files of Rubrene peroxide crystals. This material is available free of charge via the Internet at http://pubs.acs.org.

■ AUTHOR INFORMATION

Corresponding Author

*E-mail address: marcello.campione@unimib.it.

■ ACKNOWLEDGMENT

Prof. Torsten Fritz (Friedrich-Schiller-Universität Jena) is kindly acknowledged for the critical reading of the paper. Dr. Silvia Rizzato (Università degli Studi di Milano) is kindly acknowledged for X-ray data collections. The financial support of Fondazione Cariplo (through Grant Nos. 2007/5205 and 2009/2551) is acknowledged.

■ REFERENCES

(1) Braga, D.; Horowitz, G. *Adv. Mater.* **2009**, *21*, 1473–1486.
(2) Muccini, M. *Nat. Mater.* **2006**, *5*, 605–613.
(3) Rand, B. P.; Genoe, J.; Heremans, P.; Poortmans, J. *Prog. Photovoltaics* **2007**, *15*, 659–676.
(4) Podzorov, V.; Menard, E.; Borissov, A.; Kiryukhin, V.; Rogers, J. A.; Gershenson, M. E. *Phys. Rev. Lett.* **2004**, *93*, 086602.
(5) Campione, M. *J. Phys. Chem. C* **2008**, *112*, 16178–16181.
(6) Zeng, X.; Wang, L.; Duan, L.; Qiu, Y. *Cryst. Growth Des.* **2008**, *8*, 1617–1622.
(7) Li, Z.; Du, J.; Tang, Q.; Wang, F.; Xu, J.-B.; Yu, J. C.; Miao, Q. *Adv. Mater.* **2010**, *22*, 3242–3246.
(8) Hochstrasser, R. M.; Ritchie, M. *Trans. Faraday Soc.* **1956**, *52*, 1363.
(9) Kytka, M.; Gerlach, A.; Schreiber, F.; Kováč, J. *Appl. Phys. Lett.* **2007**, *90*, 131911.
(10) Mitrofanov, O.; Lang, D. V.; Kloc, C.; Wikberg, J. M.; Siegrist, T.; So, W.-Y.; Sergent, M. A.; Ramirez, A. P. *Phys. Rev. Lett.* **2006**, *97*, 16601.
(11) Käfer, D.; Witte, G. *Phys. Chem. Chem. Phys.* **2005**, *7*, 2850.
(12) Najafov, H.; Mastrogiovanni, D.; Garfunkel, E.; Feldman, L. C.; Podzorov, V. *Adv. Mater.* **2011**, *23*, 981–985.
(13) Erkoç, S. *J. Mol. Struct.: THEOCHEM* **2002**, *578*, 99–101.
(14) Song, X.; Wang, L.; Fan, Q.; Wu, Y.; Wang, H.; Liu, C.; Liu, N.; Zhu, J.; Qi, D.; Gao, X.; Wee, A. T. S. *Appl. Phys. Lett.* **2010**, *97*, 032106.
(15) Tsetseris, L.; Pantelides, S. T. *Phys. Rev. B* **2008**, *78*, 115205.
(16) Krellner, C.; Haas, S.; Goldmann, C.; Pernstich, K. P.; Gundlach, D. J.; Batlogg, B. *Phys. Rev. B* **2007**, *75*, 245115.
(17) Zhang, K. K.; Tan, K.; Zou, C.; Wikberg, M.; McNeil, L. E.; Mhaisalkar, S. G.; Kloc, C. *Org. Electron.* **2010**, *11*, 1928–1934.
(18) So, W.-Y.; Wikberg, J. M.; Lang, D. V.; Mitrofanov, O.; Kloc, C. L.; Siegrist, T.; Sergent, A. M.; Ramirez, A. P. *Solid State Commun.* **2007**, *142*, 483–486.
(19) Campione, M.; Moret, M.; Raimondo, L.; Sassella, A. *J. Phys. Chem. C* **2009**, *113*, 20927–20933.
(20) Nonnenmacher, M.; O'Boyle, M. P.; Wickramasinghe, H. K. *Appl. Phys. Lett.* **1991**, *58*, 2921.
(21) Palermo, V.; Palma, M.; Samorì, P. *Adv. Mater.* **2006**, *18*, 145–164.
(22) Luo, Y.; Gustavo, F.; Henry, J.-Y.; Mathevet, F.; Lefloch, F.; Sanquer, M.; Rannou, P.; Grévin, B. *Adv. Mater.* **2007**, *19*, 2267–2273.
(23) Kloc, C.; Simpkins, P. G.; Siegrist, T.; Laudise, R. A. *J. Cryst. Growth* **1997**, *182*, 416–427.
(24) Campione, M.; Cartotti, M.; Pinotti, E.; Sassella, A.; Borghesi, A. *J. Vac. Sci. Technol. A* **2004**, *22*, 482.
(25) Liscio, A.; Palermo, V.; Gentilini, D.; Nolde, F.; Müllen, K.; Samorì, P. *Adv. Funct. Mater.* **2006**, *16*, 1407–1416.
(26) Klapetek, P.; Nečas, D.; Anderson, C. *Gwyddion User Guide*; 2004.
(27) Burla, M. C.; Caliandro, R.; Camalli, M.; Carrozzini, B.; Cascarano, G. L.; De Caro, L.; Giacovazzo, C.; Polidori, G.; Spagna, R. *J. Appl. Crystallogr.* **2005**, *38*, 381–388.
(28) Sheldrick, G. *SHELXL-97—Programme for Structure Refinement*; University of Göttingen: Göttingen, Germany, 1997.
(29) Spek, A. L. *J. Appl. Crystallogr.* **2003**, *36*, 7–13.
(30) Frisch, M. J.; Trucks, G. W.; Schlegel, H. B.; Scuseria, G. E.; Robb, M. A.; Cheeseman, J. R.; Montgomery, J. A.; Vreven, T.; Kudin, K. N.; Burant, J. C.; Millam, J. M.; Iyengar, S. S.; Tomasi, J.; Barone, V.; Mennucci, B.; Cossi, M.; Scalmani, G.; Rega, N; Petersson, G. A.; Nakatsuji, H.; Hada, M.; Ehara, M.; Toyota, K.; Fukuda, R.; Hasegawa, J.; Ishida, M.; Nakajima, T.; Honda, Y.; Kitao, O.; Nakai, H.; Klene, M.; Li, X.; Knox, J. E.; Hratchian, H. P.; Cross, J. B.; Bakken, V.; Adamo, C.; Jaramillo, J.; Gomperts, R.; Stratmann, R. E.; Yazyev, O.; Austin, A. J.; Cammi, R.; Pomelli, C.; Ochterski, J. W.; Ayala, P. Y.; Morokuma, K.; Voth, G. A.; Salvador, P.; Dannenberg, J. J.; Zakrzewski, V. G.; Dapprich, S.; Daniels, A. D.; Strain, M. C.; Farkas, O.; Malick, D. K.; Rabuck, A. D.; Raghavachari, K.; Foresman, J. B.; Ortiz, J. V.; Cui, Q.; Baboul, A. G.; Clifford, S.; Cioslowski, J.; Stefanov, B. B.; Liu, G.; Liashenko, A.; Piskorz, P.; Komaromi, I.; Martin, R. L.; Fox, D. J.; Keith, T.; Al-Laham,

M. A.; Peng, C. Y.; Nanayakkara, A.; Challacombe, M.; Gill, P. M. W.; Johnson, B.; Chen, W.; Wong, M. W. Gonzalez, C.; Pople, J. A. Gaussian 03, Revision D.02, Gaussian, Inc.: Wallingford, CT, 2004.

(31) Jurchescu, O. D.; Meetsma, A.; Palstra, T. *Acta Crystallogr., Sect. B: Struct. Sci.* **2006**, *62*, 330–334.

(32) Cleveland, J. P.; Anczykowski, B.; Schmid, A. E.; Elings, V. B. *Appl. Phys. Lett.* **1998**, *72*, 2613.

(33) Liscio, A.; Palermo, V.; Samorì, P. *Adv. Funct. Mater.* **2008**, *18*, 907–914.

(34) Ellison, D. J.; Lee, B.; Podzorov, V.; Frisbie, C. D. *Adv. Mater.* **2011**, *23*, 502–507.